

# A near-global climatology of oceanic coherent eddies

**Josué Martínez-Moreno<sup>1</sup>, Andrew McC. Hogg<sup>1</sup>, and Matthew H. England<sup>2</sup>**

<sup>1</sup>Research School of Earth Science and ARC Center of Excellence for Climate Extremes, Australian National University, Canberra, Australia

<sup>2</sup>Climate Change Research Centre (CCRC), UNSW Australia, Sydney NSW, Australia

## Key Points:

- Coherent eddies contain around 50% of the surface ocean kinetic energy budget.
- Seasonal cycle of the number of coherent eddies and coherent eddy amplitude reveal a 3-6 month lag to wind forcing.
- The seasonal lag between the number and the amplitude of coherent eddies suggests a role for the inverse cascade.

---

Corresponding author: Josué Martínez-Moreno, [josue.martinezmoreno@anu.edu.au](mailto:josue.martinezmoreno@anu.edu.au)

12 **Abstract**

13 Ocean eddies influence regional and global climate through mixing and transport of heat  
14 and properties. One of the most recognizable and ubiquitous feature of oceanic eddies  
15 are coherent vortices with spatial scales of tens to hundreds of kilometers, frequently re-  
16 ferred as “mesoscale eddies”. Coherent mesoscale eddies are known to transport prop-  
17 erties across the ocean and to locally affect near-surface wind, cloud properties and rain-  
18 fall patterns. Although coherent eddies are ubiquitous, their climatology, seasonality and  
19 long-term temporal evolution remains poorly understood. Here, we examine the kinetic  
20 energy contained by coherent eddies and present the seasonal, inter-annual and long-term  
21 variability of automatically identified coherent eddies from satellite observations from  
22 1993 to 2019. Around 50% of the kinetic energy contained by ocean eddies corresponds  
23 to coherent eddies. Additionally, a strong seasonal cycle is observed, with a 3–6 months  
24 lag between the wind forcing and the response of the coherent eddy field. The season-  
25 ality of the number of coherent eddies and their amplitude reveals that the number of  
26 coherent eddies responds faster to the forcing ( $\sim$ 3 months), than the coherent eddy am-  
27 plitude (which is lagged by  $\sim$ 6 months). **Regional analysis ...** Our analysis highlights  
28 the relative importance of the coherent eddy field in the ocean kinetic energy budget,  
29 implies a strong response of the eddy number and eddy amplitude to forcing at differ-  
30 ent time-scales, and showcases the seasonality, and multidecadal trends of coherent eddy  
31 properties.

32 **Plain language summary**

33 Coherent eddies are the most common feature of ocean variability observable from  
34 satellites. They are crucial in ocean dynamics as they can transport properties over long  
35 distances and interact with the atmosphere. Our study investigates the seasonal, inter-  
36 annual, and long-term changes in the abundance and intensity of coherent eddies, by au-  
37 tomatically identifying individual eddies over the available satellite altimeter record. The  
38 seasonal cycle suggests a transition from numerous, smaller, and weaker coherent eddies,  
39 to fewer and larger, and stronger coherent eddies over the season. In addition, a long-  
40 term adjustment of the coherent eddy field is identified with possible links to long-term  
41 changes in the climate system.

42      **1 Introduction**

43      Mesoscale ocean variability with spatial scales of tens to hundreds of kilometers is  
 44      comprised of processes such as vortices, waves, and jets (Ferrari & Wunsch, 2009; Fu et  
 45      al., 2010). These mesoscale processes are highly energetic, and they play a crucial role  
 46      in the transport of heat, salt, momentum, and other tracers through the ocean (Wun-  
 47      sch & Ferrari, 2004; Wyrtki et al., 1976; Gill et al., 1974). One of the most recognizable  
 48      and abundant ocean processes observable from space are mesoscale vortices. Although  
 49      mesoscale vortices are commonly referred to in the literature as “mesoscale eddies”, this  
 50      term is also often used to describe the total mesoscale ocean variability (the time-varying  
 51      component of the mesoscale flow), thus, to avoid ambiguity we will refer to mesoscale  
 52      vortices as *coherent eddies*.

53      Coherent eddies are quasi-circular geostrophic currents. According to their rota-  
 54      tional direction, the sea surface height anomaly within a coherent eddy can have a neg-  
 55      ative or positive sea surface height anomaly (cold-core and warm-core coherent eddies,  
 56      respectively). This characteristic sea surface height signature of coherent eddies has been  
 57      utilized to identify and track coherent eddies from satellite altimetry (e.g., Chelton et  
 58      al., 2007; Faghmous et al., 2015; Ashkezari et al., 2016; Martínez-Moreno et al., 2019;  
 59      Cui et al., 2020). Automated identification algorithms of coherent eddies have revealed  
 60      their ubiquity in the oceans, with a predominant influence at hotspots of eddy activity  
 61      such as in boundary current extensions and the Antarctic Circumpolar Current. In these  
 62      regions, it has been estimated that coherent eddies contribute around 40–50% of the net  
 63      mesoscale kinetic energy (Chelton et al., 2011) and thus a significant fraction of the to-  
 64      tal kinetic energy (Ferrari & Wunsch, 2009). Although this estimate showcases the im-  
 65      portance of the mesoscale coherent eddy field, the energy contained by coherent eddies  
 66      was estimated by extracting the total geostrophic velocity within the radius of each de-  
 67      tected coherent eddy; thus, it is possible that this estimate may contain energy from other  
 68      processes. **Here we extend on this past work by reconstructing the surface im-**  
 69      **print of the coherent eddies ...** Coherent eddies are abundant and energetic; there-  
 70      fore they are also essential to ocean dynamics as concluded by many previous studies (Hogg  
 71      & Blundell, 2006; Siegel et al., 2011; Beron-Vera et al., 2013; Frenger et al., 2013, 2015;  
 72      Pilo et al., 2015; Schubert et al., 2019; Patel et al., 2020).

73 There is broad consensus that mesoscale eddy kinetic energy has a pronounced sea-  
74 sonal variability (Qiu, 1999; Qiu & Chen, 2004; Kang & Curchitser, 2017; Uchida et al.,  
75 2017). Several hypotheses have been proposed to explain this seasonality including: sea-  
76 sonal variations of atmospheric forcing (Sasaki et al., 2014), seasonality of the mixed layer  
77 depth (Qiu et al., 2014; Callies et al., 2015), seasonality of the intensity of barotropic in-  
78 stability (Qiu & Chen, 2004), the variability of the baroclinic instability due to the sea-  
79 sonality of the vertical shear (Qiu, 1999), and a seasonal lag of the inverse energy cas-  
80 cade (i.e. energy is transported between scales, from small to large; Arbic et al., 2013)  
81 in combination with the presence of a front in the mixed layer, which can lead to a sea-  
82 sonal cycle of the baroclinic instability (Qiu et al., 2014). On one hand, processes such  
83 as barotropic and baroclinic instabilities control the seasonality of coherent eddies in the  
84 ocean. On the other hand, recent studies using observations and eddy-permitting climate  
85 models suggest several long-term adjustments of the global ocean capable of long-term  
86 changes in the coherent eddy field. Such readjustments include a multidecadal increase  
87 in the ocean stratification resulting from temperature and salinity changes (Li et al., 2020),  
88 a horizontal readjustment of sea surface temperature gradients (Cane et al., 1997; Bouali  
89 et al., 2017; Ruela et al., 2020), and an intensification of the kinetic energy, eddy kinetic  
90 energy, and mesoscale eddy kinetic energy over the last 3 decades as a consequence of  
91 an increase in wind forcing (Hu et al., 2020; Wunsch, 2020; Martínez-Moreno et al., 2021).  
92 All these seasonal factors and long-term readjustments directly influence the annual and  
93 decadal response of the coherent eddy field, however, the seasonality of the coherent com-  
94 ponent of the eddy kinetic energy, as well as the seasonal cycle and trends of the coher-  
95 ent eddy statistics, remain unknown.

96 Here we present a new global climatology of the coherent eddy kinetic energy by  
97 reconstructing the coherent eddy signature from satellite observations. Our study doc-  
98 uments the seasonal cycle of the coherent eddy kinetic energy, and the seasonal cycle and  
99 long-term trends of the coherent eddy properties over the satellite record. Moreover, we  
100 conduct more detailed analyses in regions where coherent eddies dominate the eddy ki-  
101 netic energy field. The rest of this paper is structured as follows: the data sources and  
102 methodology are described in Section 2. Then, we present the climatology, energy ra-  
103 tios, and global seasonality of the coherent eddy kinetic energy in Section 3. Section 4  
104 outlines the global climatology and seasonality of coherent eddy properties, followed by  
105 long-term changes of the coherent eddy properties (Section 5). Then we focus our at-

106 tention on the seasonal cycle and coherent eddy properties in regions dominated by co-  
 107 herent eddies (Section 6). Finally, Section 7 summarizes the main results and discusses  
 108 the implications of this study.

109 **2 Methods**

110 We use daily sea surface height (SSH) data made available by the Copernicus Ma-  
 111 rine Environment Monitoring Service in near real time (CMEMS, 2017). This gridded  
 112 product contains the sea surface height and geostrophic velocities with daily  $0.25^\circ$  res-  
 113 olution from January 1993 to 2019. The daily geostrophic velocities allow us to compute  
 114 the kinetic energy (KE) and eddy kinetic energy (EKE) over the satellite record. The  
 115 main source of EKE is the time-varying wind (Ferrari & Wunsch, 2009); thus, we also  
 116 compute the seasonal cycle of the wind magnitude from the JRA55 reanalysis (Japan  
 117 Meteorological Agency, Japan, 2013) using wind velocities at 10m above the ocean's sur-  
 118 face.

119 Over the same record, coherent eddy statistics from Martínez-Moreno et al. (2019),  
 120 hereafter MM19, are analyzed and compared with those released by Chelton & Schlax  
 121 (2013), hereafter CS13. Both datasets are gridded in a  $1^\circ$  resolution and are produced  
 122 via automated eddy identification algorithms using closed contours of SSH. However, these  
 123 datasets have important differences in the criteria they use to identify and record coher-  
 124 ent eddies statistics. The major differences include: (i) MM19's algorithm requires an  
 125 adjustment between a 2D Gaussian and the SSH anomaly (SSHa) surface within the iden-  
 126 tified closed contour, while CS13's only uses the outermost closed contour of SSH; (ii)  
 127 MM19's dataset reports the maximum SSHa within the identified coherent eddy, while  
 128 CS13's algorithm reports the maximum SSH value minus the discrete level in which the  
 129 coherent eddy was identified; and (iii) MM19's dataset includes all detected coherent ed-  
 130 dies, while CS13's dataset excludes coherent eddies with lifetimes shorter than four weeks  
 131 and coherent eddy amplitudes smaller than 1cm. Moreover, MM19's algorithm allows  
 132 the reconstruction of the coherent eddy field under the assumption that coherent eddies  
 133 have a 2D Gaussian imprint in the sea surface height. This Gaussian reconstruction of  
 134 the coherent eddy field then allows us to estimate the coherent geostrophic eddy veloc-  
 135 ities and thus the kinetic energy contained only by coherent eddies.

136            **2.1 Kinetic Energy decomposition**

137            Kinetic energy is commonly divided into the mean and time-varying components  
 138            through a Reynolds decomposition. At a given time, the surface velocity field  $\mathbf{u} = (u, v)$   
 139            is split into the time mean ( $\bar{\mathbf{u}}$ ) and time varying components ( $\mathbf{u}'$ ). Moreover, MM19 pro-  
 140            posed to further decompose the eddy kinetic energy into the energy contained by coher-  
 141            ent features ( $\mathbf{u}'_e$ ) and non-coherent features ( $\mathbf{u}'_n$ ). Therefore the KE equation can be writ-  
 142            ten as:

$$\text{KE} = \underbrace{\bar{u}^2 + \bar{v}^2}_{\text{MKE}} + \underbrace{u'^2_e + v'^2_e}_{\text{CEKE}} + \underbrace{u'^2_n + v'^2_n}_{\text{nCEKE}} + \mathcal{O}_c^2 + \mathcal{O}^2 \quad (1)$$

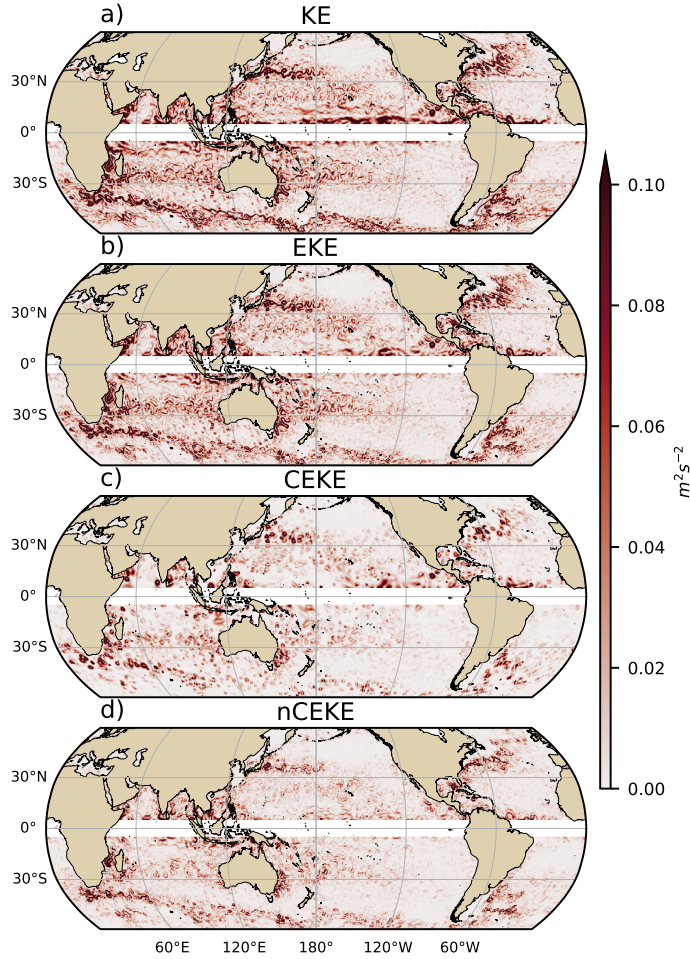
EKE

143            Due to the properties of this decomposition, the second order term  $\mathcal{O}^2$  is zero when  
 144            averaged over the same period as  $\bar{\mathbf{u}}$ . However,  $\mathcal{O}_c^2$  is not necessarily negligible, unless it  
 145            is averaged over time and space. More information about the decomposition of the field  
 146            into coherent features and non-coherent features is explained in Martínez-Moreno et al.  
 147            (2019). A global snapshot of each component of kinetic energy decomposition is shown  
 148            in Figure 1, where the KE and EKE are comprised of rings and filaments. As expected,  
 149            the decomposition of EKE into CEKE and nCEKE components exhibits only ring-like  
 150            signatures expected of coherent eddies, while the non-coherent component shows primar-  
 151            ily filaments, with some mis-identified coherent eddies.

155            **2.2 Eddy statistics**

156            The eddy statistics used in this study include (i) the eddy count ( $c\text{Eddy}_n$ ) defined  
 157            as the number of coherent eddies per grid cell, (ii) the eddy diameter defined as the di-  
 158            ameter of a circle with equal area to the closed contour of each identified eddy, and (iii)  
 159            the mean eddy amplitude defined as the mean amplitude of the coherent eddies within  
 160            the cell ( $c\text{Eddy}_{amp}$ ). The latter metric can be separated into positive ( $c\text{Eddy}_{amp}^+$ ) and  
 161            negative ( $c\text{Eddy}_{amp}^-$ ) coherent eddy amplitudes, defined as the mean amplitude of warm  
 162            core and cold core coherent eddies, respectively, within the cell. The polarity indepen-  
 163            dent eddy amplitude ( $|c\text{Eddy}_{amp}|$ ) is defined as:

$$|c\text{Eddy}_{amp}| = \frac{1}{2} (c\text{Eddy}_{amp}^+ - c\text{Eddy}_{amp}^-) \quad (2)$$



152 **Figure 1.** Snapshot of surface kinetic energy ( $\overline{KE}$ ), surface eddy kinetic energy ( $\overline{EKE}$ ),  
 153 surface coherent eddy kinetic energy ( $\overline{CEKE}$ ), and surface non-coherent eddy kinetic energy  
 154 ( $\overline{nCEKE}$ ) for the 1st of January 2017.

164 Note that the  $cEddy_{amp}^+$  and  $cEddy_{amp}^-$  are sign definite, thus the difference will always  
 165 be positive, whereas the gridded averaged  $cEddy_{amp}$  can be negative or positive noting  
 166 the dominant polarity of coherent eddies in the region, and the absolute  $cEddy_{amp}$  is de-  
 167 noted by  $|cEddy_{amp}|$ . We analyze the climatology and trends of the above eddy statis-  
 168 tics over the available satellite record, namely between 1993 and 2019. We exclude the  
 169 equatorial region ( $10^\circ S - 10^\circ N$ ) and regions poleward of  $60^\circ$ , **because the geostrophic**  
 170 **approximation is invalid near the equator and the satellite spatial coverage**  
 171 **at high-latitudes is unable to resolve the coherent eddy scales polewards of**  
 172  **$60^\circ$ .** Note that the climatology of  $cEddy_n$  is computed by adding all the identified ed-

173 dies over the record, while all other climatological statistics are computed as the time-  
 174 average over the record. Seasonal climatologies are calculated for the monthly average  
 175 of each coherent eddy statistic, while hemispherical time-series are filtered with a run-  
 176 ning average of 90 days. Trends of  $cEddy_n$  and  $|cEddy_{amp}|$  are calculated by coarsen-  
 177 ing the dataset to a  $5^\circ$  grid, and then linear trends are computed for each grid point. The  
 178 statistical significance of trends is assessed by a modified Mann-Kendall test (Yue & Wang,  
 179 2004).

180 Time averages are denoted by  $\overline{\quad}$ , while area-weighted averages are denoted using  
 181  $\langle \quad \rangle$ , where the area-weighted average of a function  $f$  is:

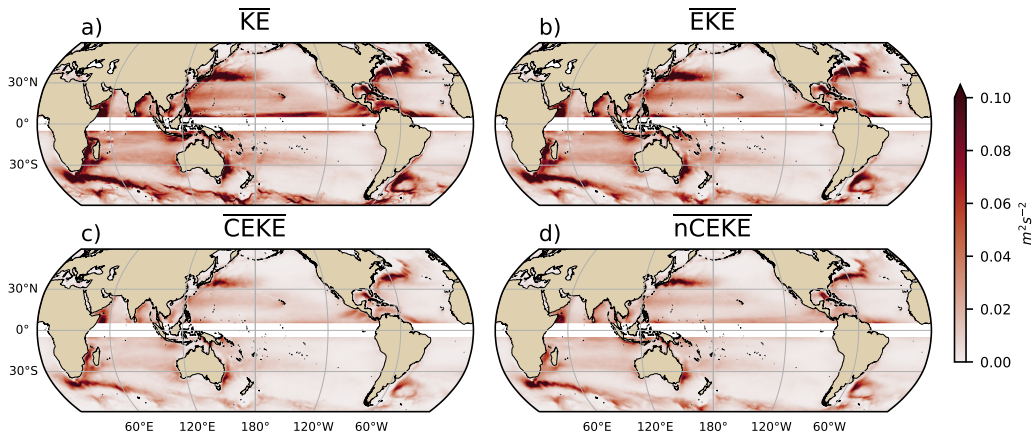
$$\langle f \rangle = \frac{\int f \xi dx dy}{\int \xi dx dy}, \quad (3)$$

182 Where  $\xi$  is a mask that is set to zero in grid cells where no coherent eddies were iden-  
 183 tified.

### 184 3 Global Coherent Eddy Energetics

185 The kinetic energy decomposition estimated from sea surface height measured by  
 186 satellite altimeters averaged from 1993-2019 is shown in Figure 2. These maps show that  
 187 many regions of the global ocean are highly energetic in mean KE ( $\overline{KE}$ ), mean EKE ( $\overline{EKE}$ ),  
 188 mean coherent eddy kinetic energy ( $\overline{CEKE}$ ) and mean non-coherent eddy kinetic energy  
 189 ( $\overline{nCEKE}$ ). The spatial pattern highlights well-known regions of the ocean where mesoscale  
 190 processes are abundant, such as the western boundary current extensions (WBCe) and  
 191 the Antarctic Circumpolar Current. The spatial distribution of the energy contained by  
 192 the reconstructed mesoscale coherent eddies and non-coherent components are similar  
 193 (Figures 2c,d). However, there are some regions where coherent eddies dominate over  
 194 non-coherent, and vice-versa. Overall, this decomposition suggests that boundary cur-  
 195 rent extensions and other energetic regions of the ocean, particularly eddy-rich regions,  
 196 contain both coherent and non-coherent components of the kinetic energy.

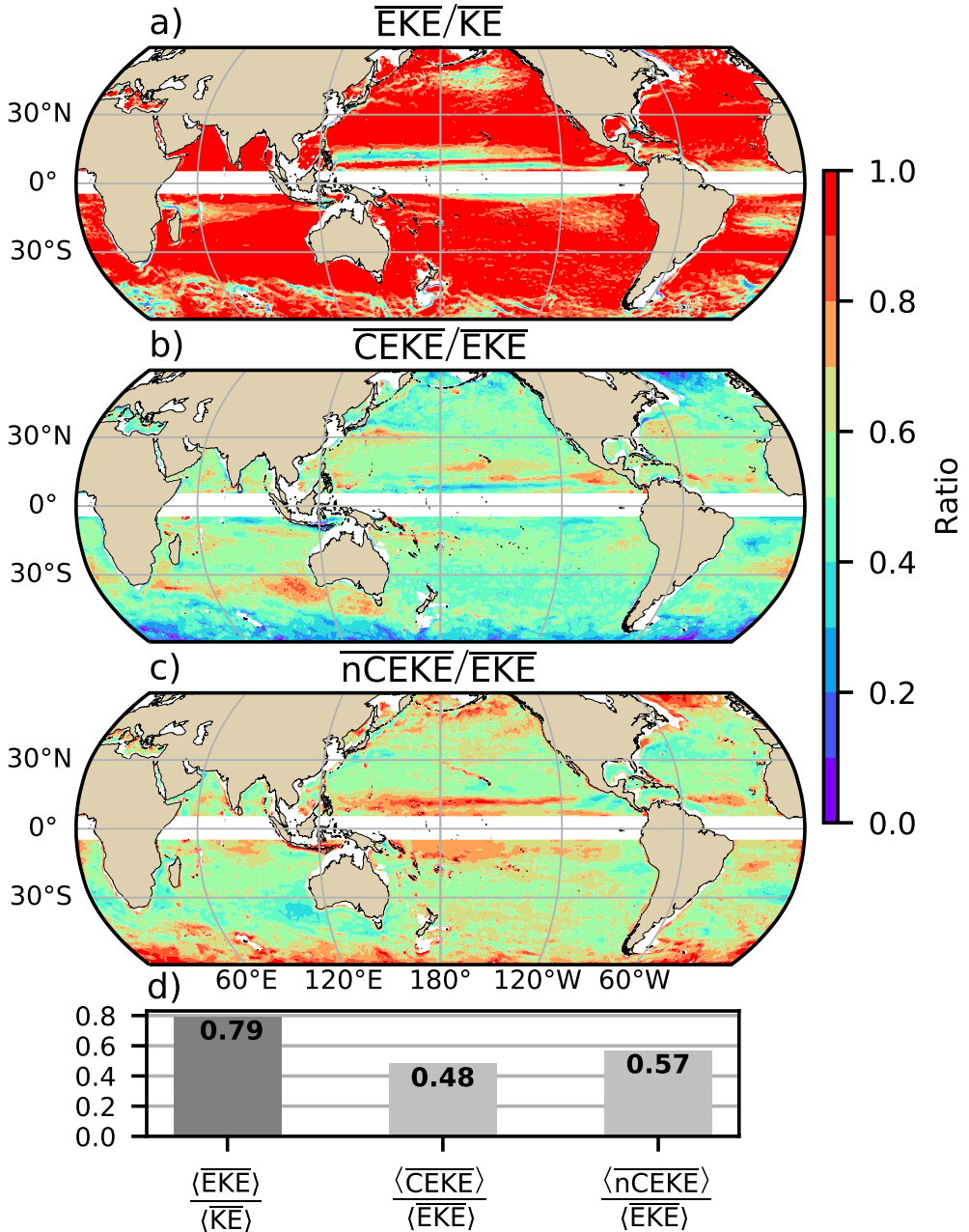
200 Eddy kinetic energy is known to be more than an order of magnitude greater than  
 201 kinetic energy of the mean flow (MKE; Gill et al. 1974); this result is clearly shown in  
 202 Figure 3a, where  $\overline{EKE}$  is responsible for almost all the  $\overline{KE}$  across the ocean, except for  
 203 regions with persistent currents over time. Such regions are located in the mean bound-  
 204 ary extension locations, the equatorial Pacific currents and regions in the Antarctic Cir-  
 205 cumpolar Current, where the  $\overline{EKE}$  explains around 40% of the  $\overline{KE}$ . In a previous study,



197 **Figure 2.** Mean surface kinetic energy ( $\overline{KE}$ ), surface eddy kinetic energy ( $\overline{EKE}$ ), surface  
 198 coherent eddy kinetic energy ( $\overline{CEKE}$ ), and surface non-coherent eddy kinetic energy ( $\overline{nCEKE}$ )  
 199 averaged between 1993-2018.

215 Chelton et al. (2011) estimated that the EKE within coherent eddies with lifetimes greater  
 216 than 4 weeks contain between 40-60% of the  $\overline{EKE}$ . Our method to reconstruct the co-  
 217 herent eddy signature (Figure 3b) further corroborates that the coherent eddy compo-  
 218 nent ( $\langle \overline{CEKE} \rangle$ ) has ~48% of the  $\langle \overline{KE} \rangle$  (Figure 3d). Furthermore, global area averages  
 219 of the ratios show that  $\langle \overline{EKE} \rangle$  explains ~78% of the ocean  $\langle \overline{KE} \rangle$  field, while non coherent  
 220 eddy features contain ~57% percent of the  $\langle \overline{EKE} \rangle$ . Note that the globally averaged  
 221 coherent and non coherent components do not add to 100% as the cross terms ( $O_c^2$ ) are  
 222 non-zero and coherent eddy reconstruction errors. The spatial pattern reveals a dom-  
 223 inance of the  $\overline{CEKE}$  equatorward from the boundary current extensions and in areas with  
 224 large coherent eddy contributions of around 80% of the region's eddy kinetic energy, such  
 225 as south of Australia, in the Tehuantepec Gulf, and in the tropical Atlantic. An evident  
 226 signal is a reduction of the energy contained by coherent eddies at high latitudes and an  
 227 increase in the energy explained by non-coherent eddies; this signal could be a consequence  
 228 of the inability of the  $0.25^\circ$  satellite resolution ( $\sim 13$  km at  $60^\circ$  latitude) to resolve co-  
 229 herent eddies with scales smaller than  $\sim 10$  km (first baroclinic Rossby radius at  $60^\circ$ ; Chel-  
 230 ton et al. 1998).

231 Figure 4 shows the seasonal cycle of the area weighted EKE and CEKE for the North-  
 232 ern Hemisphere ( $\langle EKE \rangle_{NH}$  and  $\langle CEKE \rangle_{NH}$ ;  $10^\circ N - 60^\circ N$ ) and Southern Hemisphere  
 233 ( $\langle EKE \rangle_{SH}$  and  $\langle CEKE \rangle_{SH}$ ;  $60^\circ S - 10^\circ S$ ). In both hemispheres, the  $\langle EKE \rangle$  and  $\langle CEKE \rangle$



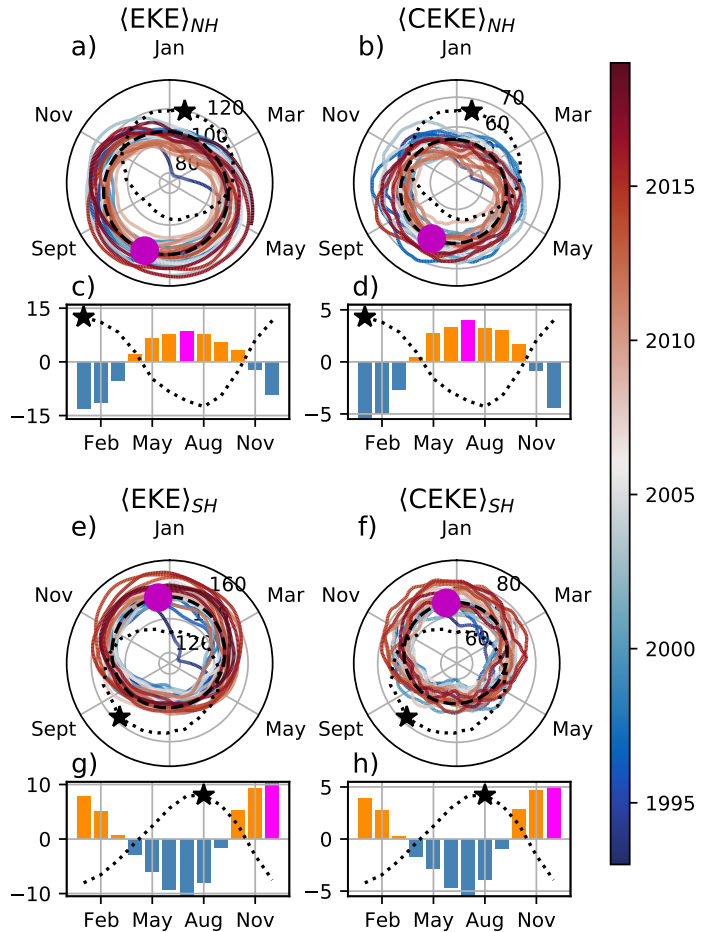
200 **Figure 3.** Ratios of the kinetic energy components. a) Map of the proportion of mean eddy  
 201 kinetic energy ( $\overline{EKE}$ ) versus mean kinetic energy ( $\overline{KE}$ ); b) Map of the percentage of mean co-  
 202 herent eddy kinetic energy ( $\overline{CEKE}$ ) versus mean eddy kinetic energy ( $\overline{EKE}$ ); c) Map of the  
 203 percentage of mean non-coherent eddy kinetic energy ( $\overline{nCEKE}$ ) versus mean eddy kinetic energy  
 204 ( $\overline{EKE}$ ); d) Global time and area averaged (represented by  $\langle \rangle$ ) percentage of mean eddy kinetic  
 205 energy ( $\langle \overline{EKE} \rangle$ ) versus the global mean kinetic energy ( $\langle \overline{KE} \rangle$ ), area averaged percentage of mean  
 206 coherent eddy kinetic energy ( $\langle \overline{CEKE} \rangle$ ) and mean non coherent eddy kinetic energy ( $\langle \overline{nCEKE} \rangle$ )  
 207 versus global mean eddy kinetic energy ( $\langle \overline{EKE} \rangle$ ). Regions where the depth of the ocean is shall-  
 208 lower than 1000m are removed from the ratio estimation.

peak during summer. In the Northern Hemisphere, the largest  $\langle \text{EKE} \rangle_{NH}$  and  $\langle \text{CEKE} \rangle_{NH}$  occurs in July,  $\sim 6$  months after the maximum winds in January (purple bar and back star in Figure 4c and d). Meanwhile, the Southern Ocean  $\langle \text{EKE} \rangle_{SH}$  and  $\langle \text{CEKE} \rangle_{SH}$  seasonal maxima arises during December,  $\sim 4$  months after the maximum winds in August (purple bar and back star in Figure 4g, and h). This lag between winds and the eddy and coherent eddy energy components is further discussed in Section 4.

The cyclic plots in Figure 4 show the temporal evolution of  $\langle \text{EKE} \rangle$  and  $\langle \text{CEKE} \rangle$ . Note that high frequency variability can be observed in the  $\langle \text{CEKE} \rangle$  field with temporal scales of a few months, this variability could be attributed to regional dynamics averaged over the hemisphere (boundary currents, ocean gyres, etc.), as well as errors within the coherent eddy reconstruction. Additionally, concentric changes in the cyclic plots highlight long-term changes over the record. For example, the Northern Hemisphere winters during early years of the record (blue) had a more energetic coherent eddy field, which has transitioned to weaker coherent energy content since 2010 (red), in other words, the intensity of the  $\langle \text{CEKE} \rangle_{NH}$  field has decreased. A larger long-term change can be observed in the Southern Hemisphere, where concentric growth over time in  $\langle \text{EKE} \rangle_{SH}$  and  $\langle \text{CEKE} \rangle_{SH}$  support the previously observed strengthening of the eddy field in the Southern Ocean (Hogg et al., 2015; Martínez-Moreno et al., 2019; Martínez-Moreno et al., 2021).

## 4 Global Coherent Eddy Statistics

Coherent eddy kinetic energy allows us to quantify and study the energy of the eddy field, but the coherent eddy properties computed by automated coherent eddy identification algorithms allow us to further investigate in more detail the contribution and temporal changes of their abundance (i.e. the number of eddies) and their intensity (both their amplitude and diameter). Figure 5 shows gridded climatologies of the number of eddies and the eddy amplitude. In this analysis, we contrast our MM19 eddy count with that of CS13 (Chelton et al., 2007; Figure 5a-b). Although the number of identified eddies is larger in MM19, possibly due to the lifespan filter implemented by CS13, both datasets reveal consistent spatial patterns. For example, both datasets show high abundance of eddies in the East North Pacific, East North Atlantic, as well as the East South Pacific, East South Atlantic and East Indian Ocean, and fewer eddies in the tropics and at higher latitudes ( $\sim 60^\circ$ ). An interesting pattern also emerges in both eddy count datasets, where small scale structures emerge in the eddy count field. These small structures high-



252 **Figure 4.** Seasonality of the area-weighted eddy kinetic energy ( $\langle EKE \rangle$ ) and coherent eddy ki-  
 253 netic energy ( $\langle CEKE \rangle$ ). Panels a) and b) show the time-series of the Northern Hemisphere, while  
 254 panels e) and f) correspond to the Southern Hemisphere. Panels c) and d) show the seasonal  
 255 cycle of the  $\langle EKE \rangle_{NH}$  and  $\langle CEKE \rangle_{NH}$  in the Northern Hemisphere, and panels g) and h) show  
 256 the Southern Hemisphere ( $\langle EKE \rangle_{SH}$  and  $\langle CEKE \rangle_{SH}$ ). Dashed lines correspond to the seasonal  
 257 cycle of the fields and dotted lines show the seasonal cycle of the wind magnitude smoothed over  
 258 120 days (moving average). The black and magenta markers (circle and bar) show the maximum  
 259 of the seasonal cycle for the kinetic energy components and the wind magnitude, respectively. In  
 260 the cyclic plots, line colors shows the year.

275 light preferred coherent eddy paths observable in boundary current extensions and over  
 276 regions of the Southern Ocean. These structures and paths of coherent eddies could be  
 277 associated with topographic features, with overall consistency between the eddy count  
 278 patterns using the two different eddy identification methods.

284 Regions with large counts of eddies have in general small absolute amplitudes (Figure  
 285 5 c). The ocean gyre interiors have a larger absolute amplitude and finally regions  
 286 such as the boundary current extensions and the Antarctic Circumpolar Current have  
 287 the largest coherent eddy absolute amplitudes, as shown also by Chelton et al. (2011).  
 288 Eddy amplitude highlights regions dominated by a given coherent eddy polarity, for ex-  
 289 ample, boundary extensions have a preferred sign (Figure 5 d); namely, positive ampli-  
 290 tude polewards of the boundary current extension mean location, and negative ampli-  
 291 tude equatorwards. This sign preference is consistent with the preferential way that co-  
 292 herent eddies are shed from boundary current extensions; with warm core eddies (pos-  
 293 itive) polewards of the boundary current extension, and equatorward for cold core ed-  
 294 dies (negative) (Kang & Curchitser, 2013; Chelton et al., 2011, 2007). These global statis-  
 295 tics reveal the absolute coherent eddy amplitude as a proxy for the CEKE with similar  
 296 spatial patterns (Figure 2 & Figure 5c) and showcases that regions where  $\overline{\text{CEKE}}$  has a  
 297 large proportion of  $\overline{\text{EKE}}$  (Figure 3), the absolute coherent eddy amplitude is also large.

298 To further understand the seasonal cycle of  $\langle \text{CEKE} \rangle$ , we compute the climatology  
 299 of coherent eddy properties in each hemisphere (Figure 6). The seasonality of the num-  
 300 ber of eddies in the Northern Hemisphere peaks in April (Figure 6a, c), while the South-  
 301 ern Hemisphere maximum number of eddies occurs during October (Figure 6e, g). Mean-  
 302 while, the seasonality of the eddy amplitude ( $\langle |c\text{Eddy}_{amp}| \rangle$ ) peaks in August and Jan-  
 303 uary for the Northern and Southern Hemispheres respectively (Figure 6b, d, f, and h).  
 304 As expected, the seasonality of  $\langle |c\text{Eddy}_{amp}| \rangle$ , equivalent to the intensity of the coher-  
 305 ent eddies, is consistent with the seasonal cycle of  $\langle \text{CEKE} \rangle$ .

306 A key feature of Figure 6 is a distinct lag of  $\sim 3$  months between the winds and eddy  
 307 count, while the eddy amplitude maximum occurs  $\sim 6$  months after the seasonal max-  
 308 ima in winds. We suggest that the eddy number increases earlier in the year and, through  
 309 eddy-eddy interactions (merging of coherent eddies), the amplitude of the coherent eddy  
 310 increases  $\sim 3$  months after. This seasonal lag and summer maxima is consistent with pre-  
 311 vious studies which suggest that a time-lag of the inverse cascade (Sasaki et al., 2014;

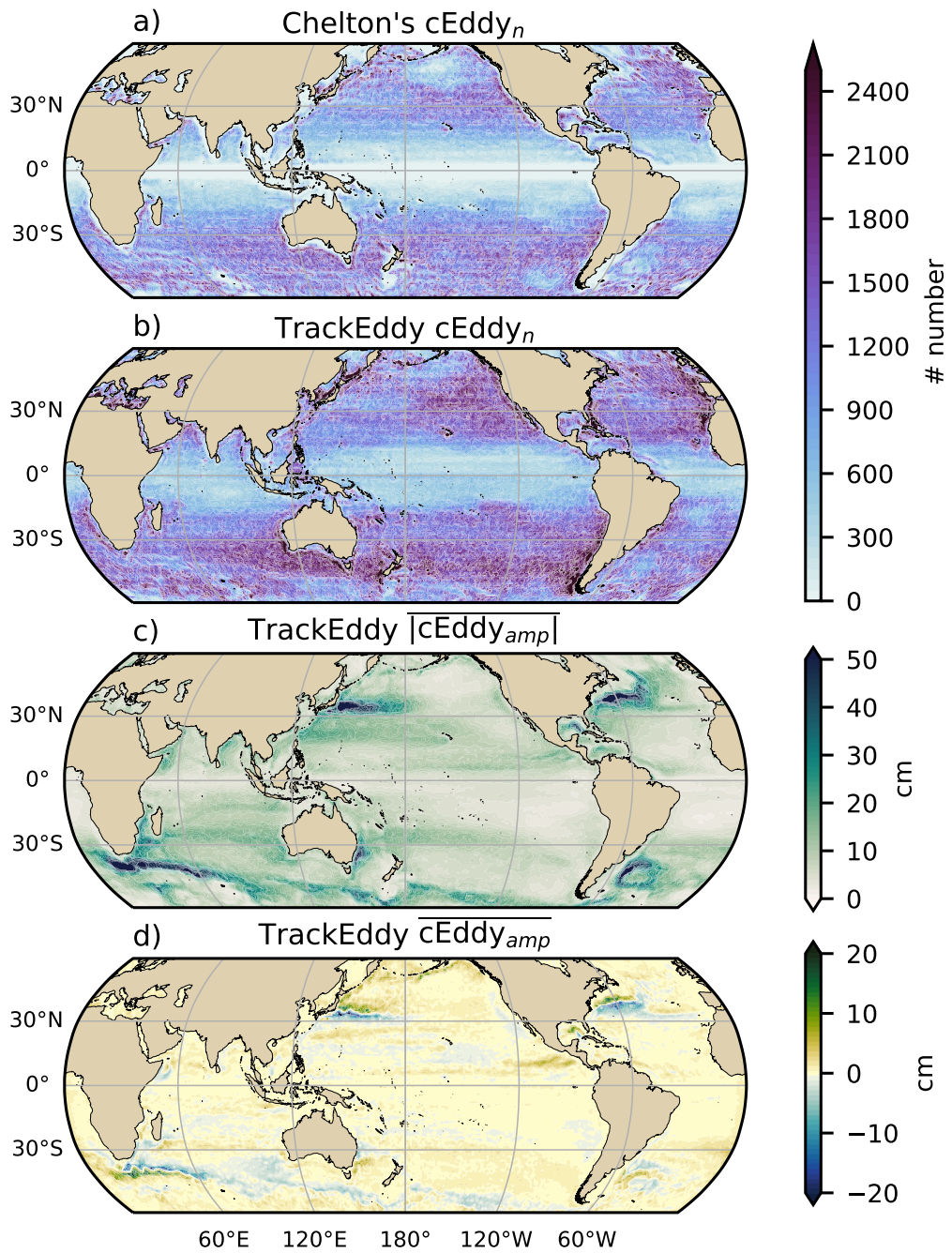
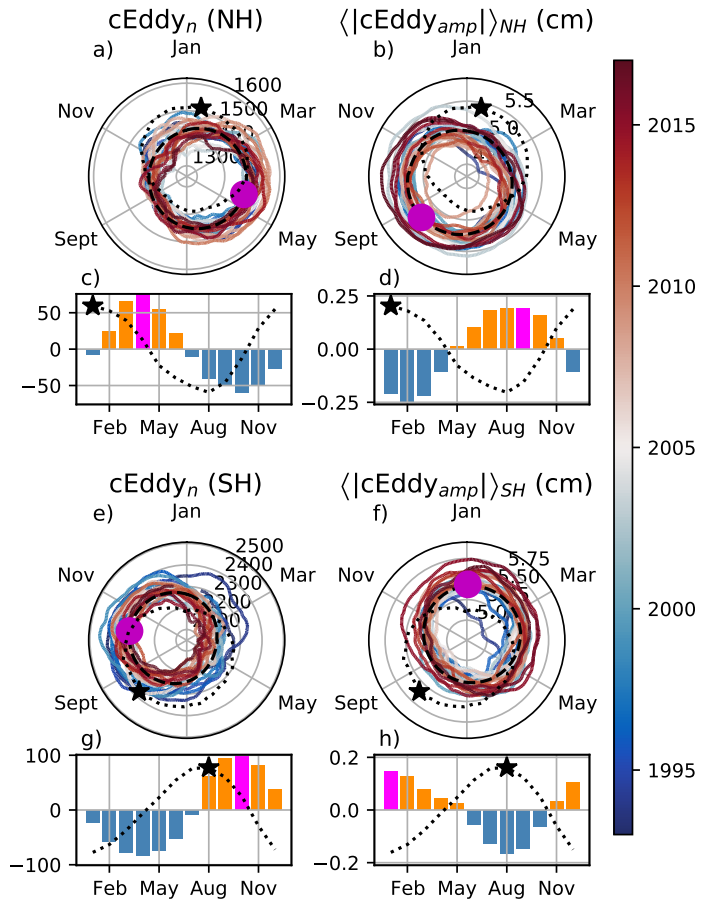


**Figure 5.** Averaged coherent eddy statistics. a) Climatology of the number of coherent eddies ( $cEddy_n$ ) identified by Chelton et al. (2007); b) Climatology of the number of coherent eddies ( $cEddy_n$ ) identified by Martínez-Moreno et al. (2019); c) Climatology of the mean absolute coherent eddy amplitude ( $cEddy_{amp}$ ). d) Climatology of the mean coherent eddy amplitude ( $cEddy_{amp}$ ).

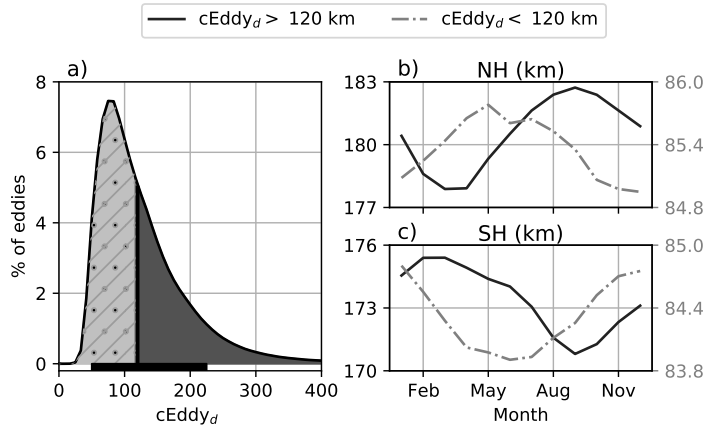
312 Qiu et al., 2014) is responsible for the EKE seasonal cycle, where winter has the high-  
 313 est energy at the smallest scales (non-resolvable with satellite observations), spring and  
 314 autumn have the highest and lowest energy at scales of 50-100 km, and summertime has  
 315 the highest energy at the largest scales ( $> 100$  km; Uchida et al. 2017). Thus, the max-  
 316 imum of  $\langle \text{EKE} \rangle$ ,  $\langle \text{CEKE} \rangle$ , and  $\langle |c\text{Eddy}_{amp}| \rangle$  located during summertime suggests that  
 317 the seasonality of eddies and coherent eddies could be dominated by scales larger than  
 318 100 km.

319 This result can be further explored by looking at the seasonal evolution of the eddy  
 320 diameter ( $c\text{Eddy}_d$ ). Note that 90% of identified coherent eddies have diameters between  
 321 50 to 220 km (Figure 7a). We partition eddies into large-scale coherent eddies (diam-  
 322 eter  $> 120$  km) and small-scale coherent eddies (diameter  $< 120$  km; Figure 7a). In the  
 323 Northern Hemisphere, small-scale eddies have a seasonal peak in diameter during May,  
 324 while large-scale eddies have the greatest diameter in September (Figure 7b). Meanwhile,  
 325 in the Southern Hemisphere, the small-scale coherent eddies exhibit maximum dia-  
 326 meter in December, while the diameter of large-scale coherent eddies peaks in February (Fig-  
 327 ure 7 c). This result suggests that wind driven baroclinic instabilities generate small co-  
 328 herent eddies early in the season, which then merge and grow to become larger in diam-  
 329 eter and amplitude, and thus, more energetic. This process is likely associated with the  
 330 inverse energy cascade, and suggests that this mechanism not only drives EKE season-  
 331 ality, but also may be responsible for the seasonal cycle of coherent eddies.

332 Long-term changes can be observed in Figure 6a,b, e, and f where growing/shrinking  
 333 concentric circles over time denote an increase/decrease trend of the field. This trend  
 334 is particularly evident in the Southern Hemisphere, where the number of eddies has de-  
 335 creased, while the eddy amplitude has increased. This result is consistent with the ob-  
 336 served trends in EKE and mesoscale EKE in the Southern Ocean (Hogg et al., 2015; Martínez-  
 337 Moreno et al., 2019). The coherent eddy amplitude from positive coherent eddies and  
 338 negative coherent eddies show similar seasonal cycles to the absolute eddy amplitude.  
 339 The Northern Hemisphere decrease in absolute eddy amplitude is driven by a decrease  
 340 of the amplitude of negative coherent eddies in the Northern Hemisphere. Meanwhile  
 341 in the Southern Ocean, the increase in absolute eddy amplitude is corroborated by a strength-  
 342 ening of both coherent eddy polarities since the early 90s.



343 **Figure 6.** Seasonality of the count of number of eddies ( $c\text{Eddy}_n$ ) and the area-weighted polar-  
 344 ity independent coherent eddy amplitude ( $\langle |c\text{Eddy}_{amp}| \rangle$ ); Panels a and b show the time-series of  
 345 the Northern Hemisphere, while panels e and f correspond to the Southern Hemisphere. Panels c  
 346 and d show the seasonal cycle of the  $c\text{Eddy}_n$  and  $\langle |c\text{Eddy}_{amp}| \rangle_{NH}$  in the Northern Hemisphere,  
 347 and panels g and h show the Southern Hemisphere  $c\text{Eddy}_n$  and  $\langle |c\text{Eddy}_{amp}| \rangle_{SH}$ . Dashed lines  
 348 correspond to the seasonal cycle of the fields and dotted lines show the seasonal cycle of the  
 349 wind magnitude, smoothed over 120 days (moving average). The black and magenta markers  
 350 (circle and bar) indicate the maximum of the seasonal cycle for the eddy property, and the wind  
 351 magnitude, respectively. In the cyclic plots, line colors show the year from 1993-2019.

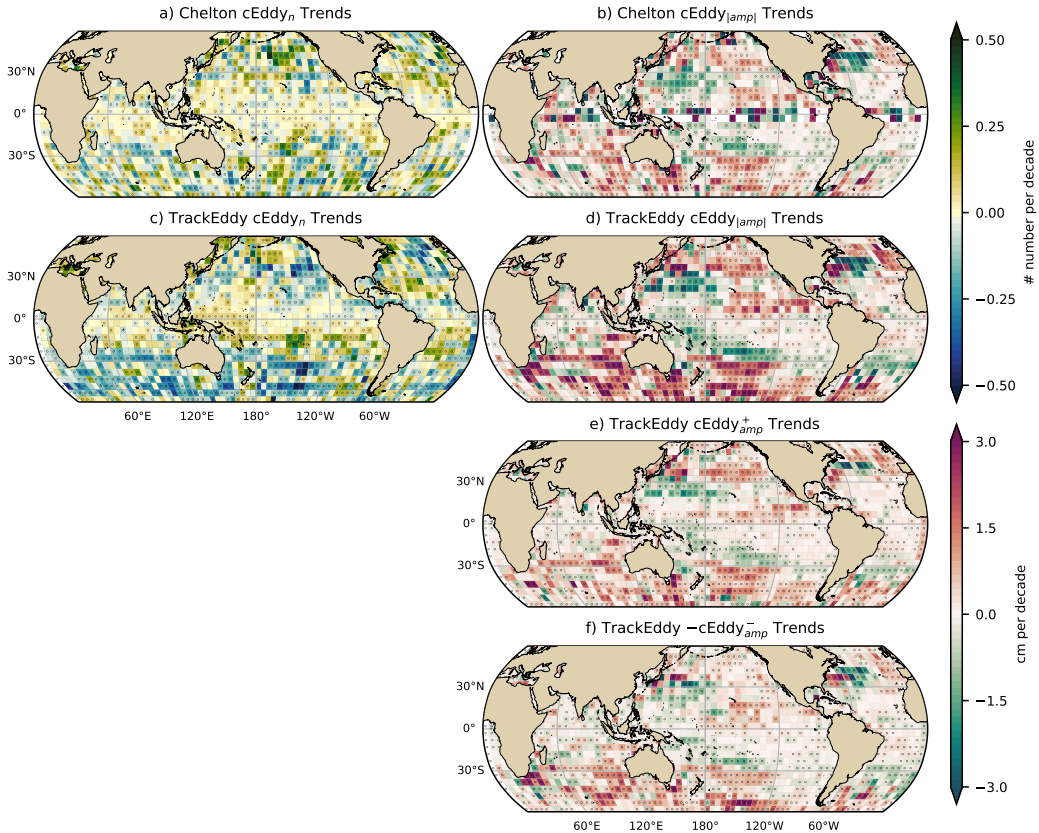


352 **Figure 7.** Distribution of the identified eddy diameter ( $cEddy_d$ ; km) and hemispherical  
 353 seasonality of the coherent eddy diameter. a) Distribution in percentage of identified eddy am-  
 354 plitude, solid bar below distribution represents 90% of the identified eddies. Seasonal cycle of  
 355 the eddy diameter for the b) Northern Hemisphere and c) Southern Hemisphere. Dark solid line  
 356 and area corresponds to coherent eddies with diameters larger than 120 km, while light gray  
 357 dash-dotted line and area shows coherent eddies with diameters smaller than 120 km.

## 358 5 Trends

359 The results presented in Figures 4 and 6 suggest a long-term readjustment of the  
 360 coherent eddy field. The long-term trends of the number of coherent eddies, absolute co-  
 361 herent eddy amplitude, and coherent eddy amplitude polarities are further explored in  
 362 Figure 8 contrasting the MM19 and CS13 methods. MM19 and CS13 datasets show con-  
 363 sistent spatial patterns in the trends and significance of the number of coherent eddies  
 364 and the absolute coherent eddy amplitude. Several regions in the ocean, such as the South-  
 365 ern Ocean, North Atlantic and North Pacific, show a decrease in the number of eddies.  
 366 Those same regions also have a clear increase in the absolute coherent eddy amplitude.  
 367 These trends are similar to those observed in mesoscale eddy kinetic energy (Martínez-  
 368 Moreno et al., 2021) and provide additional evidence of a readjustment of the mesoscale  
 369 eddy field over the last 3 decades.

370 The observed trends of  $cEddy_{amp}$  in several oceanic regions have the same scale  
 371 as sea level rise ( $\sim 3\text{cm}$  per decade). By analyzing the positive and negative coherent eddy  
 372 amplitude, we filter out the observed trends that come from a net increase in sea level.  
 373 In fact, each coherent eddy polarity has intensified in the Southern Ocean and North East



380 **Figure 8.** Trends of coherent eddy statistics. a) and b) Trends of the number of identified  
 381 coherent eddies from satellite observations identified using the TrackEddy scheme of MM19,  
 382 and those reported in CS13's dataset. c) and d) Trends of the absolute value of identified coherent  
 383 eddy amplitude ( $cEddy_{amp}$ ) from satellite observations identified using TrackEddy (after  
 384 MM19), and those reported by CS13. e) and f) Trends of the eddy amplitude polarity using  
 385 TrackEddy ( $cEddy_{amp}^+$  and  $cEddy_{amp}^-$ ). Gray stippling shows regions that are statistically signifi-  
 386 cant above the 95% confidence level.

374 Pacific and Atlantic. In other words, the amplitude of each polarity has increased over  
 375 time, and thus this strengthening is an intrinsic response of the coherent eddy field. Note  
 376 that the negative coherent eddy amplitude dominates the global  $|cEddy_{amp}|$  trends (Figure  
 377 8e, f). However, different trend patterns can be observed in both positive and neg-  
 378 ative coherent eddy amplitudes in the North Atlantic and North Pacific, where the neg-  
 379 ative coherent eddy amplitude in the Western Boundary Currents appears to decrease.

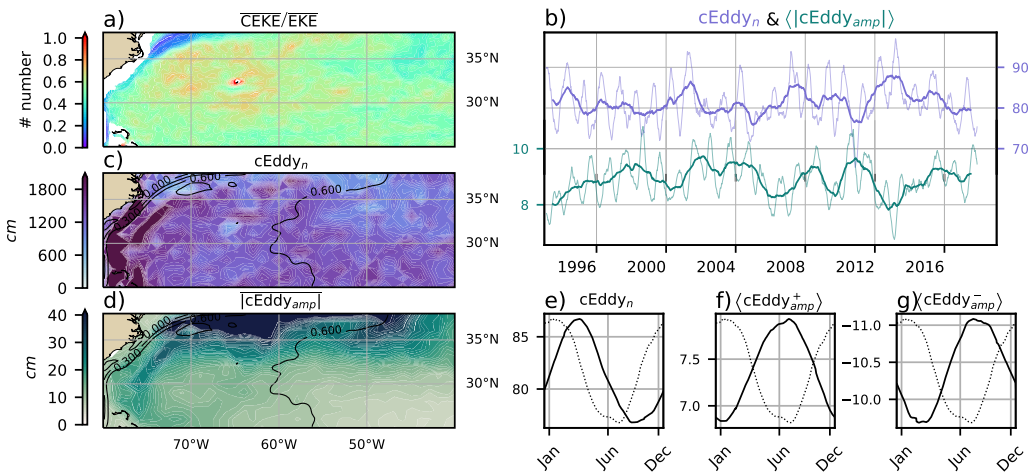
387     **6 Regional Climatology**

388     For regions with relatively large proportions of CEKE located at WBCe and east-  
 389     ern boundary currents, we investigate the seasonal and long-term variability of the co-  
 390     herent eddy properties. The most energetic WBCe include the Gulf Stream, the Kuroshio  
 391     Current, and the Agulhas Current (Figures 9, 10, and 11). Coherent eddy generation in  
 392     boundary current extensions occurs through baroclinic and barotropic instabilities of the  
 393     mean current, thus all these regions share similar generation dynamics. In all these re-  
 394     gions without exception; (i) CEKE contains 50-80% of the EKE in regions equatorward  
 395     from the mean WBCe, (ii) the number of eddies is consistently small over the mean WBCe  
 396     location, and (iii) the eddy amplitude is larger over the mean WBCe location.

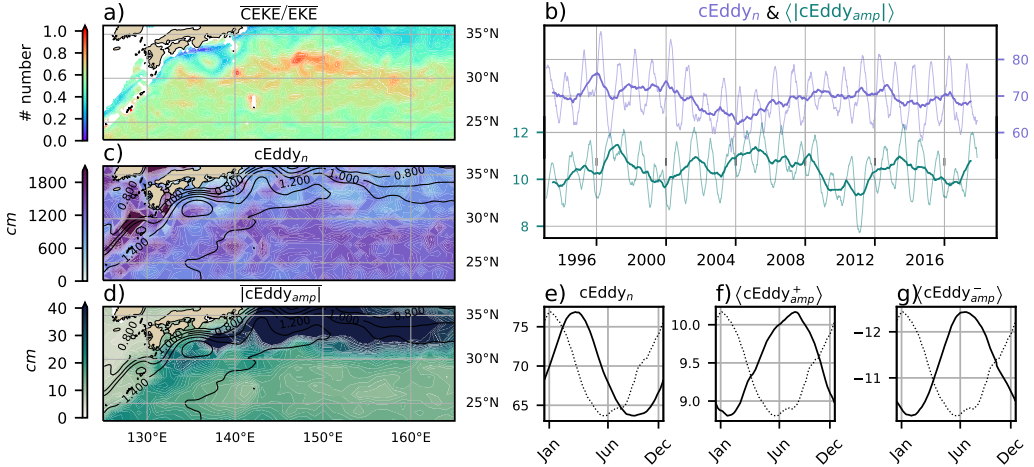
397     In the Gulf Stream, the energy ratio between CEKE and EKE is  $\sim$ 56% (Figure 9).  
 398     The highest energy ratio occurs in regions with numerous eddies, collocated with regions  
 399     where the largest  $|cEddy_{amp}|$  gradients occur. The time series of  $cEddy_n$  and  $\langle |cEddy_{amp}| \rangle$   
 400     are anti-correlated (-0.52), and they display interannual and seasonal variability. Although  
 401     Chaudhuri et al. (2009) observed that a positive phase of the North Atlantic Oscillation  
 402     (NAO) exhibits higher EKE, due to an increase in baroclinic instability, thus suggest-  
 403     ing more coherent eddies, we do not find a correlation between the  $cEddy_n$  or the  $\langle |cEddy_{amp}| \rangle$   
 404     in the Gulf Stream and the NAO index. Similar to the signal observed in the hemispheric  
 405     analysis, the eddy count seasonal cycle follows the wind maximum lagging by  $\sim$ 3 months,  
 406     while the amplitude of the coherent eddies lags by  $\sim$  6 months.

415     The variability of the  $cEddy_n$  and  $\langle |cEddy_{amp}| \rangle$  in the Kuroshio Current are weakly  
 416     anti-correlated (-0.41; Figure 10). However, on average 56% of the energy in the region  
 417     corresponds to CEKE. As observed in the Gulf Stream, there is an important seasonal  
 418     cycle in the boundary extension, where the eddy count seasonal cycle occurs in March,  
 419     lagging the wind maximum by  $\sim$ 3 months (January). Meanwhile, the amplitude of the  
 420     coherent eddies lags the wind maximum by  $\sim$  6 months (June).

427     In the Southern Hemisphere the strongest boundary current, the Agulhas Current,  
 428     shows similar behavior to its counterparts in the Northern Hemisphere (Figure 11). On  
 429     average, coherent eddies in the Agulhas current contain  $\sim$ 56% of the energy, meanwhile  
 430     the  $cEddy_n$  seasonal peak occurs in August, while the  $\langle |cEddy_{amp}| \rangle$  peak occurs in January-  
 431     February. The seasonal lag between the winds, eddy count, and eddy amplitude in each  
 432     of the WBCe is interpreted as being analogous to the lagged response of coherent eddy



407 **Figure 9.** Climatology of the eddy field and coherent eddy field in the Gulf Stream. a) Ratio  
 408 of mean coherent eddy kinetic energy ( $\overline{CEKE}$ ) versus mean eddy kinetic energy ( $\overline{EKE}$ ); b) Thick  
 409 lines show the running average over 2 years and thin lines show the running average over 90 days  
 410 of the coherent eddy number sum and the average coherent eddy amplitude; c) Map of the num-  
 411 ber of eddies; d) Map of the average coherent eddy amplitude; e) Seasonal cycle of the number  
 412 of eddies ( $cEddy_n$ ); f) Seasonal cycle of the positive coherent eddy amplitude ( $\langle cEddy_{amp}^+ \rangle$ ),  
 413 and g) Seasonal cycle of the negative coherent eddy amplitude ( $\langle cEddy_{amp}^- \rangle$ ). Contours in maps  
 414 correspond to mean sea surface height (m).

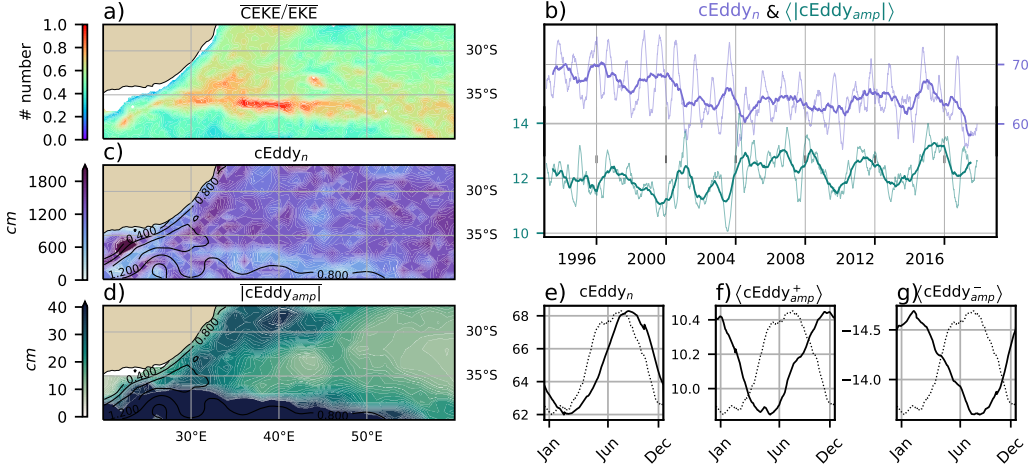


421 **Figure 10.** Climatology of the eddy field and coherent eddy field in the Kuroshio extension.  
 422 a) Ratio of mean coherent eddy kinetic energy ( $\overline{\text{CEKE}}$ ) versus mean eddy kinetic energy ( $\overline{\text{EKE}}$ );  
 423 b) Time-series of the coherent eddy number and the average coherent eddy amplitude; c) Map of  
 424 the number of eddies; d) Map of the average coherent eddy amplitude; Seasonal cycle of the e)  
 425 number of eddies; f) positive coherent eddy amplitude, and g) negative coherent eddy amplitude.  
 426 Different lines represent the same as in Figure 9.

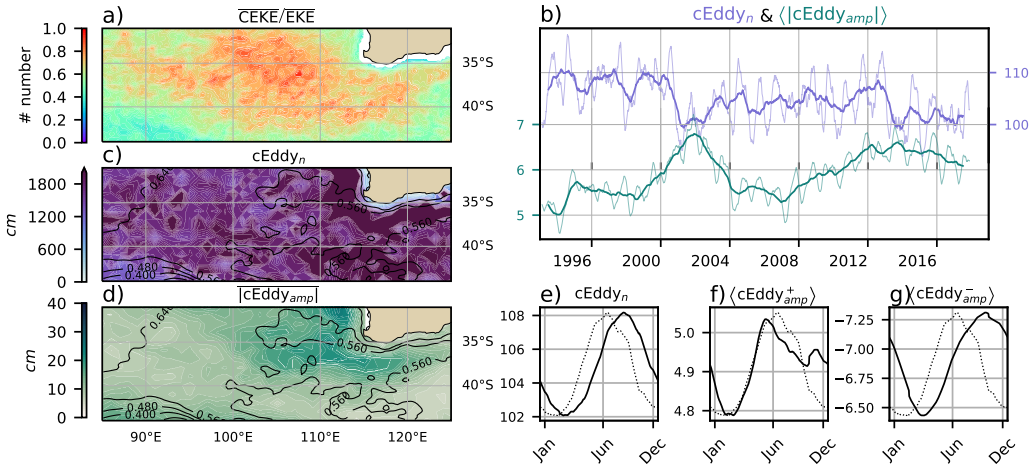
433 properties (Figure 6) due to eddy-eddy interactions, consistent with the inverse cascade  
 434 of energy.

441 Coherent eddies dominate the EKE field in other regions such as the Leeuwin Current  
 442 (Figure 12), where 65% of the energy is contained by coherent eddies. The Leeuwin  
 443 region is not characterized by having a large EKE, however, a considerable abundance  
 444 of eddies and large eddy amplitudes are observed in the region. The time-series reveal  
 445 a significant increase in the  $\langle |c\text{Eddy}_{amp}| \rangle$ , while the  $c\text{Eddy}_n$  has decreased over the last  
 446 3 decades. The seasonal cycle shows that the  $c\text{Eddy}_n$  peak occurs in August, 3 months  
 447 after the maximum winds (June). Meanwhile, the  $\langle c\text{Eddy}_{amp}^+ \rangle$  responds in synchrony  
 448 to the winds, and the  $\langle c\text{Eddy}_{amp}^- \rangle$  is in phase with the seasonal cycle of the eddy num-  
 449 ber ( $c\text{Eddy}_n$ ). Hence, this region contrast the behavior of WBCe, and showcases the spa-  
 450 tial variability of the seasonal cycle of coherent eddies.

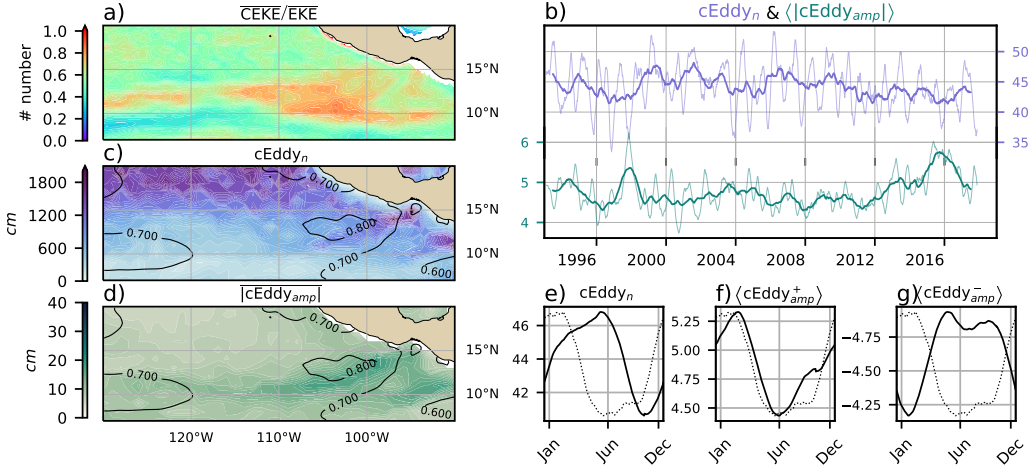
457 Another region with important contributions to the coherent eddy field is the East  
 458 Tropical Pacific (Tehuantepec region; Figure 13), where coherent eddies contain  $\sim 58\%$



435 **Figure 11.** Climatology of the eddy field and coherent eddy field in the Agulhas Current. a)  
 436 Ratio of mean coherent eddy kinetic energy ( $\overline{\text{CEKE}}$ ) versus mean eddy kinetic energy ( $\overline{\text{EKE}}$ ); b)  
 437 Time-series of the coherent eddy number and the average coherent eddy amplitude; c) Map of  
 438 the number of eddies; d) Map of the average coherent eddy amplitude; Seasonal cycle of the e)  
 439 number of eddies; f) positive coherent eddy amplitude, and g) negative coherent eddy amplitude.  
 440 Different lines represent the same as in Figure 9.



451 **Figure 12.** Climatology of the eddy field and coherent eddy field in the Leeuwin Current. a)  
 452 Ratio of mean coherent eddy kinetic energy ( $\overline{\text{CEKE}}$ ) versus mean eddy kinetic energy ( $\overline{\text{EKE}}$ ); b)  
 453 Time-series of the coherent eddy number and the average coherent eddy amplitude; c) Map of  
 454 the number of eddies; d) Map of the average coherent eddy amplitude; Seasonal cycle of the e)  
 455 number of eddies; f) positive coherent eddy amplitude, and g) negative coherent eddy amplitude.  
 456 Different lines represent the same as in Figure 9.



470 **Figure 13.** Climatology of the eddy field and coherent eddy field in the East Tropical Pacific.  
 471 a) Ratio of mean coherent eddy kinetic energy ( $\overline{\text{CEKE}}$ ) versus mean eddy kinetic energy ( $\overline{\text{EKE}}$ );  
 472 b) Time-series of the coherent eddy number and the average coherent eddy amplitude; c) Map of  
 473 the number of eddies; d) Map of the average coherent eddy amplitude; Seasonal cycle of the e)  
 474 number of eddies; f) positive coherent eddy amplitude, and g) negative coherent eddy amplitude.  
 475 Different lines represent the same as in Figure 9.

459 of the energy. In fact, coherent eddy generation in this region is modulated by winds and  
 460 coastally trapped waves which produce a strong horizontal and vertical shear (baroclinic  
 461 and barotropic instabilities; Zamudio et al., 2006). Furthermore, the equatorial gener-  
 462 ated waves propagating along the coast have an important interannual variability ob-  
 463 servable in the  $\langle |c\text{Eddy}_{amp}| \rangle$  time-series, where El Niño events are notable during 1997  
 464 and 2015 (Figure 13b). The seasonal cycle of  $c\text{Eddy}_n$ ,  $\langle c\text{Eddy}_{amp}^+ \rangle$ , and  $\langle c\text{Eddy}_{amp}^- \rangle$  sup-  
 465 port the idea of a coherent eddy response to two different coherent eddy generation mech-  
 466 anisms; the number of eddies lags by  $\sim 3$  months from the winds, while the  $\langle c\text{Eddy}_{amp}^+ \rangle$   
 467 is in phase with the winds and the time of maximum trapped wave activity (winter; Za-  
 468 mudio et al., 2006), while the  $\langle c\text{Eddy}_{amp}^- \rangle$  could be a consequence of eddy-eddy inter-  
 469 actions.

## 476 7 Discussion and Conclusions

477 We have investigated the contribution of coherent eddies to the total kinetic en-  
 478 ergy field using available satellite observations. We found that around half of the EKE

is explained by coherent eddies. This half is concentrated in eddy-rich regions where a recent multi-decadal intensification of the eddy field has been observed (Martínez-Moreno et al., 2021). The energy contained by eddies is larger than the previous estimate of 40% by Chelton et al. (2011). Although there are differences in the identification criteria of both eddy identification methods, the main cause of the difference is likely to be the lifespan and amplitude filters. These filters are widely used to track individual eddies in space and time, however, interactions between eddies in energetic regions may obscure the abundance and influence of short-lived coherent eddies. Filters are not used in this study, and indeed a lack of filters could facilitate an over-estimation of the the energy contained by coherent eddies, when mis-identifying or mis-fitting a coherent eddy.

In addition, it should be noted that regions with first baroclinic Rossby radius of deformation smaller than 10km cannot be resolved by satellite observations. Thus, the energy contained by coherent eddies around latitudes of  $60^{\circ}$  and those near the shore are missed from this estimate, and their role in the seasonal cycle and local dynamics remains unknown . New satellite altimeter missions (e.g. Surface Water and Ocean Topography; SWOT) may allow estimates of the energy contained by mesoscale coherent eddies outside the tropical region and the continental slope.

Hemisphere-wide variability indicates a strong seasonal cycle of the EKE, CEKE, and eddy properties. The seasonal cycle of the CEKE in each hemisphere occurs as a consequence of numerous small coherent eddies interacting with each other (eddy-eddy interactions) and resulting in stronger, larger and more energetic (but fewer) coherent eddies during summer, after a few months of the yearly coherent eddy number maxima. This result reveals eddy-eddy interactions and thus the transfer of energy from smaller coherent eddies to larger coherent eddies could explain the observed seasonal cycle of CEKE and coherent eddies properties.

Coherent eddy properties reveal a non-uniform long-term readjustment of the mesoscale eddy field. Overall, the eddy number has decreased globally at a significant rate of  $\sim 35$  eddies per decade from  $\sim 4000$  eddies identified globally on average each day. However, large proportions of the ocean show a strengthening of the mesoscale coherent eddy field at a rate greater than  $\sim 1$  cm per decade. This strengthening of the coherent eddy amplitude is attributed to an intensification of each coherent eddy polarity, rather than a readjustment of the coherent eddy field to sea level rise. In other words, the coherent

511 eddy amplitude intensification is occurring in both coherent eddy polarities and explains  
512 a proportion of the previously observed readjustments in the eddy field to long-term changes  
513 in the ocean forcing (Hu et al., 2020; Wunsch, 2020; Martínez-Moreno et al., 2021). This  
514 long-term readjustment reveals an intensification of the coherent eddy field, possibly due  
515 to long-term readjustments in the ocean baroclinic and barotropic instabilities, as well  
516 as the strength of the winds.

517 The reconstruction of the coherent eddies and their statistics has revealed regions  
518 with important coherent eddy contributions and a distinct seasonal evolution of the co-  
519 herent eddies. Western boundary current extensions (WBCe) generate eddies through  
520 the instability of the main currents and the seasonal cycle of coherent eddies, CEKE, and  
521 thus EKE could be associated with an inverse energy cascade observable through lagged  
522 seasonal cycles in the coherent eddy statistics. In addition, the amplitude of the seasonal  
523 cycle in WBCe is two times larger than any other region, thus the seasonality of the co-  
524 herent eddies in WBCe dominates the hemispheric seasonal cycle. Furthermore, the sea-  
525 sonal lag of the inverse energy cascade is coupled with the presence of fronts (Qiu et al.,  
526 2014), such is the case for WBCe, and our results are consistent with the notion of baro-  
527 clinic instability generating eddies and, via eddy-eddy interactions, a lagged inverse en-  
528 ergy cascade.

529 The use of satellite observations in this study limits our ability to quantify the im-  
530 portance of the inverse energy cascade seasonality in the control of the coherent eddy  
531 seasonal cycle. As mentioned above, there is robust evidence of an increase in eddy-eddy  
532 interactions, however we cannot discard important contributions from other processes  
533 such as the seasonal cycle of forcing, stratification, and instabilities, which are crucial  
534 in the generation of coherent eddies. Although this study can provide a descriptive re-  
535 sponse of the coherent eddy field, further work is needed to asses the role of eddy-  
536 eddy interactions in our changing climate, ocean dynamics, and biogeochemical process.  
537 Furthermore, the SWOT mission could allow us to advance our understanding of eddy-  
538 eddy interactions and the seasonal cycle of scales smaller than mesoscale, which may pro-  
539 vide further evidence of the inverse energy cascade driving the coherent eddy seasonal-  
540 ity.

541 **Acknowledgments**

542 Chelton & Schlax (2013) dataset was produced by SSALTO/DUACS and distributed by  
 543 AVISO+ (<https://www.aviso.altimetry.fr/>) with support from CNES, developed  
 544 and validated in collaboration with E.Mason at IMEDEA. Global coherent eddy recon-  
 545 struction, coherent and non-coherent eddy kinetic energy datasets, in addition to grid-  
 546 ded coherent eddy tracking datasets are publicly available at (<https://doi.org/10.5281/zenodo.4646429>). All analyses and figures in this manuscript are reproducible via Jupyter  
 547 notebooks and instructions can be found in the Github repository `CEKE_climatology`  
 548 ([https://github.com/josuemtzmo/CEKE\\_climatology](https://github.com/josuemtzmo/CEKE_climatology)). Trends used the Python Pack-  
 549 age `xarrayMannKendall` (<https://doi.org/10.5281/zenodo.4458776>). J.M.-M. was  
 550 supported by the Consejo Nacional de Ciencia y Tecnología (CONACYT), Mexico fund-  
 551 ing. M.H.E. is supported by the Centre for Southern Hemisphere Oceans Research (CSHOR),  
 552 a joint research centre between Qingdao National Laboratory for Marine Science and Tech-  
 553 nology (QNLM), Commonwealth Scientific and Industrial Research Organisation (CSIRO),  
 554 University of New South Wales (UNSW), and the University of Tasmania (UTAS). Anal-  
 555 yses were undertaken on the National Computational Infrastructure in Canberra, Aus-  
 556 tralia, which is supported by the Australian Commonwealth Government.  
 557

558 **References**

- 559 Arbic, B. K., Polzin, K. L., Scott, R. B., Richman, J. G., & Shriver, J. F. (2013).  
 560 On Eddy Viscosity, Energy Cascades, and the Horizontal Resolution of Gridded  
 561 Satellite Altimeter Products\*. *Journal of Physical Oceanography*, 43(2), 283–300.  
 562 doi: 10.1175/jpo-d-11-0240.1
- 563 Ashkezari, M. D., Hill, C. N., Follett, C. N., Forget, G., & Follows, M. J. (2016).  
 564 Oceanic eddy detection and lifetime forecast using machine learning methods.  
 565 *Geophysical Research Letters*, 43(23). doi: 10.1002/2016gl071269
- 566 Beron-Vera, F. J., Wang, Y., Olascoaga, M. J., Goni, G. J., & Haller, G. (2013). Ob-  
 567 jective Detection of Oceanic Eddies and the Agulhas Leakage. *Journal of Physical  
 568 Oceanography*, 43(7), 1426–1438. doi: 10.1175/JPO-D-12-0171.1
- 569 Bouali, M., Sato, O. T., & Polito, P. S. (2017). Temporal trends in sea surface tem-  
 570 perature gradients in the South Atlantic Ocean. *Remote Sensing of Environment*,  
 571 194, 100–114. doi: 10.1016/j.rse.2017.03.008
- 572 Callies, J., Flierl, G., Ferrari, R., & Fox-Kemper, B. (2015). The role of mixed-layer

- 573 instabilities in submesoscale turbulence. *Journal of Fluid Mechanics*, 788, 5–41.
- 574 doi: 10.1017/jfm.2015.700
- 575 Cane, M. A., Clement, A. C., Kaplan, A., Kushnir, Y., Pozdnyakov, D., Seager, R.,  
 576 ... Murtugudde, R. (1997). Twentieth-Century Sea Surface Temperature Trends.  
 577 *Science*, 275(5302), 957–960. doi: 10.1126/science.275.5302.957
- 578 Chaudhuri, A. H., Gangopadhyay, A., & Bisagni, J. J. (2009). Interannual variabil-  
 579 ity of Gulf Stream warm-core rings in response to the North Atlantic Oscillation.  
 580 *Continental Shelf Research*, 29(7), 856–869. doi: 10.1016/j.csr.2009.01.008
- 581 Chelton, D. B., A. d. R., Schlax, M. G., Naggar, K., & Siwertz, N. (1998). Geo-  
 582 graphical variability of the first baroclinic Rossby radius of deformation. *Journal*  
 583 *of Physical Oceanography*, 28(3), 433–460. doi: 10.1175/1520-0485(1998)028<433:  
 584 GVOTFB>2.0.CO;2
- 585 Chelton, D. B., Gaube, P., Schlax, M. G., Early, J. J., & Samelson, R. M. (2011).  
 586 The influence of nonlinear mesoscale eddies on near-surface oceanic chlorophyll.  
 587 *Science*, 334(6054), 328–32. doi: 10.1126/science.1208897
- 588 Chelton, D. B., & Schlax, M. G. (2013). *Mesoscale eddies in altimeter observations*  
 589 *of ssh*.
- 590 Chelton, D. B., Schlax, M. G., Samelson, R. M., & de Szoeke, R. A. (2007). Global  
 591 observations of large oceanic eddies. *Geophysical Research Letters*, 34(15),  
 592 L15606. doi: 10.1029/2007GL030812
- 593 CMEMS. (2017). The Ssalto/Duacs altimeter products were produced and dis-  
 594 tributed by the Copernicus Marine and Environment Monitoring Service. *Aviso*  
 595 *Dataset*. Retrieved from <https://www.aviso.altimetry.fr/>
- 596 Cui, W., Wang, W., Zhang, J., & Yang, J. (2020). Identification and census statis-  
 597 tics of multicore eddies based on sea surface height data in global oceans. *Acta*  
 598 *Oceanologica Sinica*, 39(1), 41–51. doi: 10.1007/s13131-019-1519-y
- 599 Faghmous, J. H., Frenger, I., Yao, Y., Warmka, R., Lindell, A., & Kumar, V. (2015,  
 600 6). A daily global mesoscale ocean eddy dataset from satellite altimetry. *Scientific*  
 601 *Data*, 2, 150028 EP -. doi: 10.1038/sdata.2015.28
- 602 Ferrari, R., & Wunsch, C. (2009). Ocean Circulation Kinetic Energy: Reservoirs,  
 603 Sources, and Sinks. *Annual Review of Fluid Mechanics*, 41(1), 253–282. doi: 10  
 604 .1146/annurev.fluid.40.111406.102139
- 605 Frenger, I., Gruber, N., Knutti, R., & Münnich, M. (2013). Imprint of Southern

- 606 Ocean eddies on winds, clouds and rainfall. *Nature Geoscience*, 6(8), 608 EP -.  
607 doi: 10.1038/ngeo1863
- 608 Frenger, I., Münnich, M., Gruber, N., & Knutti, R. (2015). Southern Ocean eddy  
609 phenomenology. *Journal of Geophysical Research: Oceans*, 120(11), 7413-7449.  
610 doi: 10.1002/2015JC011047
- 611 Fu, L., Chelton, D., Le Traon, P., & Oceanography, M. R. (2010). Eddy dynamics  
612 from satellite altimetry. *Oceanography*, 23(4), 14-25. doi: 10.2307/24860859
- 613 Gill, A., Green, J., & Simmons, A. (1974). Energy partition in the large-scale ocean  
614 circulation and the production of mid-ocean eddies. *Deep Sea Res Oceanogr Abstr*,  
615 21(7), 499-528. doi: 10.1016/0011-7471(74)90010-2
- 616 Hogg, A. M., & Blundell, J. R. (2006). Interdecadal variability of the southern  
617 ocean. *Journal of Physical Oceanography*, 36(8), 1626-1645. doi: 10.1175/  
618 JPO2934.1
- 619 Hogg, A. M., Meredith, M. P., Chambers, D. P., Abrahamsen, E. P., Hughes,  
620 C. W., & Morrison, A. K. (2015). Recent trends in the Southern Ocean  
621 eddy field. *Journal of Geophysical Research: Oceans*, 120(1), 257-267. doi:  
622 10.1002/2014JC010470
- 623 Hu, S., Sprintall, J., Guan, C., McPhaden, M. J., Wang, F., Hu, D., & Cai,  
624 W. (2020, 2). Deep-reaching acceleration of global mean ocean circula-  
625 tion over the past two decades. *Science Advances*, 6(6), eaax7727. doi:  
626 10.1126/sciadv.aax7727
- 627 Japan Meteorological Agency, Japan. (2013). *Jra-55: Japanese 55-year reanalysis*,  
628 *daily 3-hourly and 6-hourly data*. Boulder CO: Research Data Archive at the Na-  
629 tional Center for Atmospheric Research, Computational and Information Systems  
630 Laboratory. Retrieved from <https://doi.org/10.5065/D6HH6H41>
- 631 Kang, D., & Curchitser, E. N. (2013). Gulf stream eddy characteristics in a high-  
632 resolution ocean model. *Journal of Geophysical Research: Oceans*, 118(9), 4474-  
633 4487. Retrieved from <https://agupubs.onlinelibrary.wiley.com/doi/abs/10.1002/jgrc.20318> doi: <https://doi.org/10.1002/jgrc.20318>
- 634 Kang, D., & Curchitser, E. N. (2017). On the Evaluation of Seasonal Variability of  
635 the Ocean Kinetic Energy. *Geophysical Research Letters*, 47, 1675-1583. doi: 10  
636 .1175/JPO-D-17-0063.1
- 637 Li, G., Cheng, L., Zhu, J., Trenberth, K. E., Mann, M. E., & Abraham, J. P. (2020).

- 639 Increasing ocean stratification over the past half-century. *Nature Climate Change*,  
640 1–8. doi: 10.1038/s41558-020-00918-2
- 641 Martínez-Moreno, J., Hogg, A. M., England, M., Constantinou, N. C., Kiss, A. E.,  
642 & Morrison, A. K. (2021). Global changes in oceanic mesoscale currents over the  
643 satellite altimetry record. *Journal of Advances in Modeling Earth Systems*, 0(ja).  
644 doi: 10.1029/2019MS001769
- 645 Martínez-Moreno, J., Hogg, A. M., Kiss, A. E., Constantinou, N. C., & Morrison,  
646 A. K. (2019). Kinetic energy of eddy-like features from sea surface altime-  
647 try. *Journal of Advances in Modeling Earth Systems*, 11(10), 3090–3105. doi:  
648 10.1029/2019MS001769
- 649 Patel, R. S., Llort, J., Strutton, P. G., Phillips, H. E., Moreau, S., Pardo, P. C.,  
650 & Lenton, A. (2020). The Biogeochemical Structure of Southern Ocean  
651 Mesoscale Eddies. *Journal of Geophysical Research: Oceans*, 125(8). doi:  
652 10.1029/2020jc016115
- 653 Pilo, G. S., Mata, M. M., & Azevedo, J. L. L. (2015). Eddy surface properties and  
654 propagation at Southern Hemisphere western boundary current systems. *Ocean  
655 Science*, 11(4), 629–641. doi: 10.5194/os-11-629-2015
- 656 Qiu, B. (1999). Seasonal Eddy Field Modulation of the North Pacific Subtropical  
657 Countercurrent: TOPEX/Poseidon Observations and Theory. *Journal of Physical  
658 Oceanography*, 29(10), 2471–2486. doi: 10.1175/1520-0485(1999)029<2471:sefmot>2  
659 .0.co;2
- 660 Qiu, B., & Chen, S. (2004). Seasonal Modulations in the Eddy Field of the South  
661 Pacific Ocean. *Journal of Physical Oceanography*, 34(7), 1515–1527. doi: 10.1175/  
662 1520-0485(2004)034<1515:smitef>2.0.co;2
- 663 Qiu, B., Chen, S., Klein, P., Sasaki, H., & Sasai, Y. (2014). Seasonal Mesoscale  
664 and Submesoscale Eddy Variability along the North Pacific Subtropical Coun-  
665 tercurrent. *Journal of Physical Oceanography*, 44(12), 3079–3098. doi:  
666 10.1175/JPO-D-14-0071.1
- 667 Ruela, R., Sousa, M. C., deCastro, M., & Dias, J. M. (2020). Global and regional  
668 evolution of sea surface temperature under climate change. *Global and Planetary  
669 Change*, 190, 103190. doi: 10.1016/j.gloplacha.2020.103190
- 670 Sasaki, H., Klein, P., Qiu, B., & Sasai, Y. (2014). Impact of oceanic-scale inter-  
671 actions on the seasonal modulation of ocean dynamics by the atmosphere. *Nature*

- 672        *Communications*, 5(1), 5636. doi: 10.1038/ncomms6636
- 673        Schubert, R., Schwarzkopf, F. U., Baschek, B., & Biastoch, A. (2019). Submesoscale  
674        Impacts on Mesoscale Agulhas Dynamics. *Journal of Advances in Modeling Earth  
675        Systems*, 11(8), 2745–2767. doi: 10.1029/2019ms001724
- 676        Siegel, D., Peterson, P., DJ, M., Maritorena, S., & Nelson, N. (2011). Bio-optical  
677        footprints created by mesoscale eddies in the Sargasso Sea. *Geophysical Research  
678        Letters*, 38(13), n/a-n/a. doi: 10.1029/2011GL047660
- 679        Uchida, T., Abernathey, R., & Smith, S. (2017). Seasonality of eddy kinetic energy  
680        in an eddy permitting global climate model. *Ocean Modelling*, 118, 41-58. doi: 10  
681        .1016/j.ocemod.2017.08.006
- 682        Wunsch, C. (2020). Is The Ocean Speeding Up? Ocean Surface Energy Trends.  
683        *Journal of Physical Oceanography*, 50(11), 1–45. doi: 10.1175/jpo-d-20-0082.1
- 684        Wunsch, C., & Ferrari, R. (2004). Vertical mixing, energy, and the general circulation  
685        of the oceans. *Annual Review of Fluid Mechanics*, 36(1), 281–314. doi: 10  
686        .1146/annurev.fluid.36.050802.122121
- 687        Wyrtki, K., Magaard, L., & Hager, J. (1976). Eddy energy in the oceans. *Journal of  
688        Geophysical Research*, 81(15), 2641-2646. doi: 10.1029/JC081i015p02641
- 689        Yue, S., & Wang, C. (2004). The Mann-Kendall Test Modified by Effective Sample  
690        Size to Detect Trend in Serially Correlated Hydrological Series. *Water Resources  
691        Management*, 18(3), 201–218. doi: 10.1023/b:warm.0000043140.61082.60
- 692        Zamudio, L., Hurlbert, H. E., Metzger, E. J., Morey, S. L., O'Brien, J. J., Tilburg,  
693        C., & Zavala-Hidalgo, J. (2006). Interannual variability of Tehuantepec ed-  
694        dies. *Journal of Geophysical Research: Oceans (1978–2012)*, 111(C5). doi:  
695        10.1029/2005JC003182